



## COMPARISON OF FLUTTER ANALYSIS APPROACHES IN THE FREQUENCY DOMAIN FOR THE ECL5 OPEN FAN

**Christian Frey**

Institute of Propulsion Technology  
German Aerospace Center (DLR)  
Linder Höhe  
51147 Cologne, Germany

**Stéphane Aubert**

Ecole Centrale de Lyon, CNRS  
Université Claude Bernard Lyon 1  
INSA Lyon, LMFA, UMR5509  
69130 Ecully, France

**Renaud Daon**

SAFRAN Aircraft Engines  
77550 Moissy Cramayel, France  
renaud.daon@safrangroup.com

**Pascal Ferrand**

Ecole Centrale de Lyon, CNRS  
Université Claude Bernard Lyon 1  
INSA Lyon, LMFA, UMR5509  
69130 Ecully, France

**Valdo Pages**

SAFRAN Aircraft Engines  
77550 Moissy Cramayel, France  
valdo.pages@safrangroup.com

### ABSTRACT

The topic of this paper is the flutter analysis at part speed of the ECL5/Catana open fan. The focus is on the operating point of maximal pressure ratio on the 80% speed line, where previous studies have revealed a very high sensitivity of the aerodynamic damping for the second blade eigenmode. In particular, a sudden drop of the damping near the nodal diameters of 5 was observed with time-linearised approaches, while for harmonic balance simulations with a different solver this V-shaped spike in the damping curve was observed near the nodal diameter of 6 when a fully nonlinear setup resolving the 0th and higher harmonics was used. In the previous study, this phenomenon was related to the resonance with a convective disturbance with a characteristic circumferential speed and suggested that, if non-linear effects are taken into account, then the resonance convective speed increases.

In this paper, the flutter analyses based on three different frequency domain solvers are compared with each other: a time-linearised method and two harmonic balance solvers, each being based on different spatial schemes and/or turbulence models. The results in this paper show that the V-shaped damping curves can be reproduced with different solvers. If the zeroth harmonic is included in the set of harmonics which are solved

for then the resonance condition is located near the nodal diameter of 6, while, for frozen mean flows, it is located at 5. This behaviour is confirmed by two harmonic balance solvers.

Keywords: Aeroelasticity, CFD, Flutter, ECL5, Time-linearised Method, Harmonic Balance.

### NOMENCLATURE

$a$	vibration amplitude
$D_t$	pseudo-spectral time derivative
$\hat{D}$	time derivative in the frequency domain
$f$	frequency
$F (F^{\text{inv}})$	(inverse) Fourier transformation matrix
$F_{\text{mod}}$	modal force
$p$	static pressure
$q$	flow state
$q_s$	displacement
$k$	harmonic index
$K$	number of non-zero harmonics
$\vec{n}$	surface normal (pointing out of the fluid domain)
$N$	blade count
$\text{ND}$	nodal diameter
$N_{\text{sp}}$	number of sampling points

$R$	flow residual
$U$	relative velocity
$V$	cell volume
$W_{\text{cyc}}$	aerodynamic work per cycle
$x, \dot{x}$	mesh coordinates and velocities
$\Gamma$	blade surface
$\zeta$	aerodynamic damping ratio
$\vartheta$	circumferential coordinate
$\Psi$	mode shape
$\omega$	angular frequency
$\Omega$	rotor angular velocity
$\hat{\cdot}$	harmonic
$\cdot$	time derivative
$\text{mod}$	modal
$r$	radial
$c$	convective
AFT	alternating frequency-time domain approach
HB	harmonic balance
TM	turbulence model

## 1 INTRODUCTION

In recent years, the open fan test case ECL5/CATANA<sup>1</sup> has been studied both experimentally and numerically with a strong focus on non-synchronous coupling mechanisms between aerodynamics, acoustics and structural dynamics. The design of the ECL5 fan was thoroughly investigated with respect to potential flutter onset. During these studies, Pagès et al. found that, at 80% rotational speed, the aerodynamic damping of the second eigenmode becomes negative for the nodal diameter of 5, causing a V-shaped spike in the damping curve [1]. The minimal aerodynamic damping ratio was about  $-5.6\%$  and in apparent contradiction to both experiments and computational studies with time-domain methods [2]. It was suspected by Pagès et al. that the high negative damping is related to a so-called *convective resonance*, i.e., the combination of frequency and interblade phase angle of the blade vibration is such that it can resonate with a convective disturbance of a particular rotational speed [1]. In [3], the authors have repeated the flutter analysis for the operating point “OP-D”, but with a nonlinear frequency domain (harmonic balance). It was shown that when the harmonic balance setup corresponded to that of the time-linearised solver (one harmonic, frozen mean flow), then qualitatively similar results, in particular a spike in the damping curve, were obtained. Furthermore, the results with a truly nonlinear setup provided strong evidence of a lock-in with a contra-rotating disturbance. The results in [3] showed that while the fluid structure interaction mechanisms for this structural mode are highly nonlinear, the relative rotational speed of the disturbance could be estimated with “linearised” setups that only the first flow harmonic into account.

The aim of this paper is an in-depth comparison of the results that were obtained, on the one hand, with a steady solver and time-linearised method (elsA and turbLin) and, on the other, with the harmonic balance methods of TRACE and elsA. The aerodynamic damping ratios will be compared both globally and in terms of the contribution per area on suction and pressure sides.

## 2 CFD SOLVERS

The following section describes the CFD methods that are compared in this article. All codes are finite volume solvers that were run on multi-block structured meshes. Moreover, all unsteady simulations were based on frequency domain approaches for the URANS equations

$$\frac{\partial(V(x(t))q(t))}{\partial t} + V(t)R(x(t), \dot{x}(t), q(t)) = 0, \quad (1)$$

where,  $V$  and  $R$  denote the cell-volumes and the flow residual, respectively. In this work, the CFD solvers are applied to problems with deforming meshes which is why the dependency of  $V$  and  $R$  on the mesh coordinates  $x$  and their velocities  $\dot{x}$  is emphasised in the formula above. In the equation above,  $q$  denotes the vector of conservative variables (density, momentum density, total energy density) as well as the density variables of the turbulence model, e.g., turbulent kinetic energy density. Frozen-turbulence model approaches may give poor results for turbomachinery flutter predictions at off-design conditions [3, 4]. Hence, all CFD approaches discussed in this work will take the unsteadiness of the turbulence model quantities into account.

The frequency domain approach consists in representing time-periodic solutions to Eq. (1) by a truncated Fourier series

$$q(t) = \text{Re} \sum_{k=0}^K \hat{q}_k e^{ik\omega t}, \quad (2)$$

where  $\omega = 2\pi f$  is the angular frequency. When the cell volume is non-constant it is more convenient to work with the Fourier harmonics of the conserved quantities per cell rather than those of the mass-specific ones which means that one formulates the equations in terms of the harmonics of  $Vq$ ,

$$V(x(t))q(t) = \text{Re} \sum_{k=0}^K \widehat{(Vq)}_k e^{ik\omega t}. \quad (3)$$

Casting Eq. (1) in the frequency domain then gives

$$ik\omega \widehat{(Vq)}_k + \widehat{(VR(x, \dot{x}, q))}_k = 0, \quad k = 0, \dots, K. \quad (4)$$

<sup>1</sup>catana.ec-lyon.fr

## Frequency Domain Methods

Note that passing from the time-domain system (Eq. (1)) to its frequency domain counterpart (Eq. (4)) does not constitute a simplification other than the hypothesis that the solution is time-periodic with period  $1/f$ . The time-discretisation error introduced is the so-called *harmonic truncation error* which is due to the modelling assumption that  $Vq$  contains only  $K$  higher harmonics. The harmonic balance (HB) approach is to solve the coupled system of the  $K+1$  equations in the frequency domain. In practice, the HB approach is often combined with an alternating frequency-time (AFT) domain approach, which means that the “difficult” flow residual term  $(VR(x, \dot{x}, q))_k$  is approximated using a discrete Fourier transform of the data  $V(x(t_n))R(x(t_n), \dot{x}(t_n), q(t_n))$ , reconstructed at a finite number of sampling points  $t_j$  [5,6]. Usually, these are uniformly distributed over the period, i.e.,  $t_n = n/(fN_{\text{sp}})$ ,  $n = 0, \dots, N_{\text{sp}} - 1$ . Denoting the inverse discrete Fourier transformation matrix by  $F^{\text{inv}}$ ,

$$V(x_n)q_n = \sum_k F_{nk}^{\text{inv}} \widehat{(Vq)}_k = \text{Re} \sum_k \widehat{(Vq)}_k e^{i\omega k}$$

the discrete Fourier transformation matrix is  $F = (F^{\text{inv}})^{-1}$ . The minimal number of sampling points is  $N_{\text{sp}} = 2K + 1$  in which case  $F^{\text{inv}}$  is an invertible square matrix. If oversampling is used,  $F$  is usually defined as the Moore-Penrose inverse of  $F^{\text{inv}}$  which, in the case of equidistant sampling, gives the usual discrete forward Fourier transform.

There are two (essentially equivalent) ways of formulating AFT-based HB solvers, namely the time- and the frequency-domain approaches.

**Time-domain Harmonic Balance** The time-domain variant of harmonic balance, which is employed in elsA, means that the solutions are represented by the flow at the time instants  $t_n$ , cf. [7]. The system of equations is then

$$\omega (D_t(Vq))_n + V(x_n)R(x_n, \dot{x}_n, q_n) = 0, \quad (5)$$

where the pseudo-spectral time derivative is given by the matrix

$$D_t = F^{\text{inv}} \widehat{D} F \quad (6)$$

with the time derivative in the frequency domain,  $\widehat{D}$ , given by

$$\widehat{D} = \begin{pmatrix} 0 & 0 & 0 & \dots \\ 0 & \mathbf{i} & 0 & \dots \\ 0 & 0 & 2\mathbf{i} & \dots \\ \vdots & \vdots & \vdots & \end{pmatrix}. \quad (7)$$

This operator is applied to elements of the real vector space  $\mathbb{R} \times \mathbb{C}^K$ . Note that if  $\widehat{D}$  is to be written as a real matrix, each complex multiplication with  $\mathbf{i}$  must be replaced with the submatrix

$$\mathbf{i} \hat{=} \begin{pmatrix} 0 & -1 \\ +1 & 0 \end{pmatrix}.$$

To the best of the authors’ knowledge, all time-domain HB solvers used in turbomachinery CFD are implemented without oversampling. More details on time-domain harmonic balance solvers can be found in [7,8].

**Frequency-domain Harmonic Balance** The frequency-domain formulation [9] of harmonic balance is obtained through the multiplication of (5) with the discrete Fourier transform  $F$ , which yields

$$\omega \widehat{D} F ((V_n)(F^{\text{inv}} \widehat{q})_n + V(t_n)R(x_n, \dot{x}_n, (F^{\text{inv}} \widehat{q})_n)) = 0. \quad (8)$$

Moreover, the quantities solved are the flow harmonics  $\widehat{q}_k$  rather than the flow solution along the sampling points  $t_n$ . Note that Eq. (8) can be obtained directly from Eq. (4) by replacing all (exact) Fourier coefficients with *discrete* Fourier transforms.

In addition to the truncation error, both the time- and the frequency domain implementation exhibit an *aliasing* error which is due to the fact that for a general signal the discrete Fourier transform only approximates the true Fourier coefficients. The aliasing error can be reduced by oversampling, i.e., by choosing  $N_{\text{sp}} > 2K + 1$ , which is relatively simply to implement for a frequency domain solver [10].

The solution method for both time- and frequency-domain HB methods in CFD is usually pseudo-time marching [11].

**Time-linearised Method** The time-linearised approach is to assume that all temporal disturbances are infinitesimal, so that in Eq. (4) for  $K = 1$ , one can approximate

$$\widehat{(Vq)}_1 = \widehat{V}_0 \widehat{q}_1 + \widehat{q}_0 \frac{\partial V}{\partial x} \widehat{x}_1, \quad (9)$$

as well as

$$\begin{aligned} & \widehat{(VR(x, \dot{x}, q))}_1 \\ &= \left( \frac{\partial (VR)}{\partial x} \Big|_{(x, 0, \widehat{q}_0)} \widehat{x}_1 + \frac{\partial (VR)}{\partial \dot{x}} \Big|_{(x, 0, \widehat{q}_0)} \widehat{x}_1 + \frac{\partial (VR)}{\partial q} \Big|_{(x, 0, \widehat{q}_0)} \widehat{q}_1 \right). \end{aligned} \quad (10)$$

Since  $\hat{x}_1 = \mathbf{i}\omega\hat{x}_1$ , one obtains

$$\left(\mathbf{i}\omega\hat{V}_0 + \frac{\partial(VR)}{\partial q}\right)\hat{q}_1 = -\left(\frac{\partial(VR)}{\partial x} + \mathbf{i}\omega\frac{\partial(VR)}{\partial\dot{x}} + \mathbf{i}\omega\hat{q}_0\frac{\partial V}{\partial x}\right)\hat{x}_1. \quad (11)$$

Here, all derivatives are to be taken at  $(\hat{x}_0, 0, \hat{q}_0)$ , so for the underlying mean flow solution and the stationary background mesh. This time-averaged solution is computed beforehand using a steady solver. Whereas the HB approach results in a non-linear system of equations, the unsteady part of the time-linearised system is complex linear and can be solved with a robust Krylov method such as GMRES.

### elsA

The elsA solver has been developed by ONERA and CERFACS in close cooperation with SAFRAN. This code solves the RANS equations using a cell-centred finite volume approach [12]. Several numerical flux formulations are available of which the Roe solver [13] and the classical Jameson-Schmidt-Turkel (JST) schemes are employed in this work. Second and fourth order coefficients are set to  $\varepsilon_2 = 1/2$  and  $\varepsilon_4 = 1/32$  for the HB results below (“JST”) and to  $\varepsilon_2 = 1/2$  and  $\varepsilon_4 = 1/128$  for the modified setup (“JST (mod)”). Whereas the Roe flux is used with a van-Albada type limiter [14], the JST scheme is combined with a pressure sensor [15]. A vast range of turbulence models is available in elsA. Here, Menter’s SST [16] as well as Kok’s  $k-\omega$  [17] models are used. To prevent the well-known stagnation point anomaly, the production of turbulent kinetic energy is based on vorticity [18].

The time-domain harmonic balance method has been implemented in elsA both for aeroelasticity and rotor-stator interactions [19, 20]. Here, it is used with one harmonic only, i.e., the HB method solves from three time instants as no oversampling is used.

### TRACE

Like elsA, TRACE is a cell-centred finite volume code for the RANS equations. It has been developed for more than three decades in close cooperation with MTU Aero Engines. In this work, Roe’s numerical flux with a van Albada-type limiter and Menter’s SST model with Kato-Launder stagnation point anomaly fix [21] are used. To enhance robustness and convergence speed, the so-called  $\log\omega$ -formulation of the turbulence dissipation rate equation is used here [3, 22].

The harmonic balance solver in TRACE [10, 23, 24] is formulated in the frequency domain and has been validated for flutter simulations. As the solution fields are the harmonics, one can easily freeze the zeroth harmonic, i.e., the mean flow. Below, setups denoted by H1, H01 etc. solve for the first harmonic only,

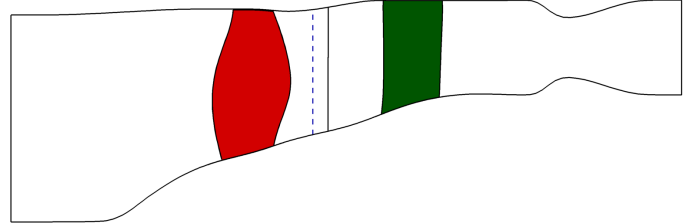


**FIGURE 1:** S2 view of rotor stator configuration. Outer boundaries and solid lines correspond to rotor and stator domains used for TRACE HB. Dashed line indicates analysis plane where radial distributions are taken.

both for the zeroth and the first, and so on. All simulations were performed with oversampling, i.e., the number of time-instants was set to  $N_{sp} = 4K + 1$ .

### Turb’Lin

The time-linearised solutions shown in this paper were obtained with Turb’Lin [25] which is a vertex-based time-linearised RANS (LRANS) solver and has been validated for transonic separated flows [25]. It should be pointed that, in contrast to the time-linearised solver in TRACE [26], the turbulence model quantities are not frozen. The turbulence model has been linearised by applying automatic differentiation to the numerical fluxes of a pre-existing RANS code [27]. The spatial scheme is the JST scheme with second and fourth order coefficients set to  $\varepsilon_2 = 1/16$  and  $\varepsilon_4 = 8$ . The linearised turbulence model equations are based on a first order accurate upstream formulation.

The underlying steady RANS flow was obtained with elsA, again with the JST scheme but with slightly different dissipation coefficients ( $\varepsilon_2 = 1/50$ ,  $\varepsilon_4 = 1$ ). Both the preliminary steady and the linearised flow solutions were obtained with Kok’s  $k-\omega$  model [28].

### 3 FAN FLUTTER CONFIGURATION

The computational domains used for TRACE HB differ from the ones for elsA and Turb’Lin in that a relatively short domain comprising both the fan and the OGV is used, see Fig. 1. The unsteady interaction with the OGV is not resolved. Rather, the role of the stator domain is to provide appropriate radial distributions of back pressures to prescribe the given mass flow. For this purpose a choked nozzle is added to the stator domain. TRACE uses both for the mean and the harmonic flows spectral 2D non-reflecting boundary conditions [29] at the inlet, outlet and the rotor-stator interface.

In contrast, the computational domains used for Turb’Lin and elsA do not resolve the OGV, but are extruded to avoid numerical reflections at the boundaries. For instance, the inlet and

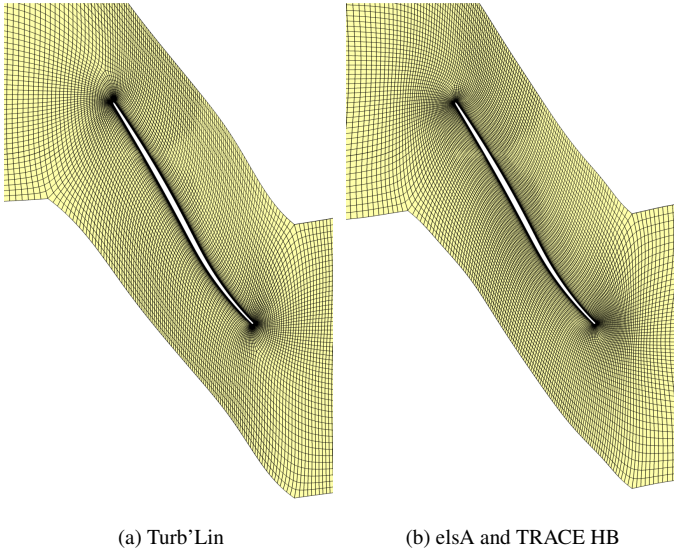


**FIGURE 2:** Mesh resolution at blade tip.

outlet of the mesh used for Turb'Lin are placed roughly 36 and 78 chord lengths away from the blade.

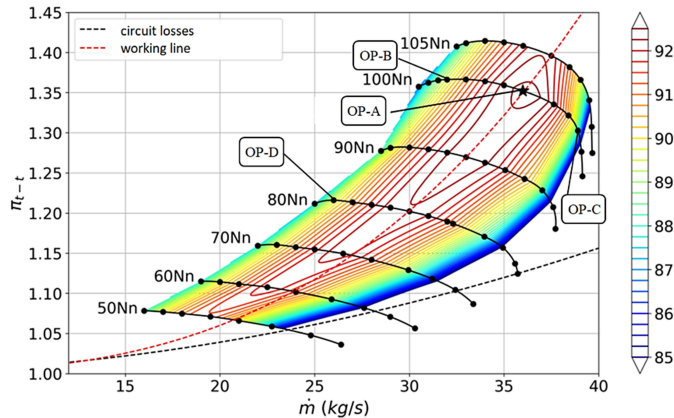


**FIGURE 3:** Fan operating map and operating point “OP-D”.

All configurations were run on block structured meshes with a low-Reynolds grid resolution near blade, hub and casing walls, i.e., with  $y+$  values close to unity. The meshes were generated with AutoGrid5. Cross sections of the meshes at the blade tip are shown in Fig. 2. While the mesh for Turb'Lin has 101 radial grid points with 21 points to resolve the tip gap, the mesh for the elsA and TRACE HB simulations is slightly finer with 133 nodes in the radial direction and 33 points in the tip gap. The grids used for the HB simulations with elsA and TRACE are identical near the fan blade and coincide there with the one used

by Fiquet et al. [2].

The operating point considered was called “OP-D” in [1] and corresponds to maximal total pressure ratio on the 80% speedline, see Fig. 3. The mass flow rate is 26 kg/s. Note that it corresponds to “OP 1” in [2].

The fan is made of composite laminate with alternating ply orientation. Details about the structure and the structural analysis can be found in [1]. The eigenmode for which flutter is

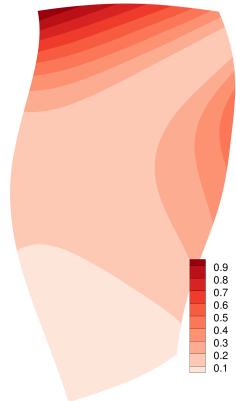


**FIGURE 4:** Displacement norm of the second blade eigenmode.

investigated is the second blade eigenmode (“Mode 2”) and depicted in Fig. 4. It has a considerable pitching component near the blade tip. The eigenfrequencies and modal masses are nearly constant [1] for all nodal diameters but ND1 which is excluded from the analysis here. The mode shape has previously been shown to depend only very slightly on the nodal diameter and is therefore to be assumed constant here.

The energy method is used for all three frequency domain solvers, i.e., the first harmonic of the flow response is computed for a small vibration amplitude  $a$  with the eigenfrequency of the corresponding nodal diameter, i.e., with a modal displacement  $q_{\text{mod}}(t) = ae^{i\omega t}$ . From this flow response, one can compute the modal work per cycle (into to the structure),

$$W_{\text{cyc}} = \int_0^{2\pi/\omega} \overline{a \dot{q}_{\text{mod}}(t)} F_{\text{mod}}(t) dt, \quad (12)$$

with the aerodynamic modal forces given by

$$F_{\text{mod}}(t) = \int_{\Gamma} \psi^H(x) p(t, x) \vec{n}(t, x) dS(x). \quad (13)$$

Here,  $\Gamma$  is the vibrating blade surface and  $\psi$  is the mode shape. The damping ratio and logarithmic decrement are obtained from

**TABLE 1:** Configurations used in this study

Solver	TM	Spatial scheme	harmonics	amplitude in mm
Turb'Lin	Kok	JST	H1	0
elsA	SST	JST	H01	0.05
elsA	SST	JST (mod.)	H01	0.05
elsA	SST	Roe	H01	0.05
TRACE	SST	Roe	H1	0.005
TRACE	SST	Roe	H1	0.05
TRACE	SST	Roe	H01	0.05
TRACE	SST	Roe	H0...5	0.05
TRACE	SST	Roe	H0...5	0.5

the real (active) part of the work per cycle using

$$\zeta = \frac{-\operatorname{Re} W_{\text{cyc}}}{4\pi a^2 E} \approx \frac{\delta}{2\pi}, \quad (14)$$

where  $E = m\omega^2/2$  is the modal energy. Whereas the harmonic balance solvers compute the time integral in Eq. (12) by summation over the sampling points, for the time-linearised method the integral is rewritten and computed from the first harmonic of the pressure and the face normal vectors, see e.g. [4].

A summary of the setups for the simulations compared in this work is given in Table 1. While the different elsA results can be used to assess the impact of the spatial discretisation scheme, the TRACE HB setups differ from each other in the vibration amplitude and the harmonics that are solved for.

#### 4 COMPARISON OF MEAN FLOWS

To estimate the influence of numerical boundary conditions, meshes, turbulence models on the mean flows, we compare first steady solutions and mean flows. Fig. 5 shows the radial distributions of total pressure and temperature ratio which are obtained from circumferential mass-weighted averages at an analysis plane. The plane is shown in Fig. 1. The agreement of the aerodynamic performance of the steady flows is quite high. Small differences, however, are noticeable at 70% and above 90% relative channel height. These differences have not been investigated further.

Figure 6 shows the streaklines for the steady elsA solution that was used for Turb'Lin and a steady TRACE solution that was obtained with the settings used for HB. Figure 7 shows streaklines for time-averaged harmonic balance results for ND5 and

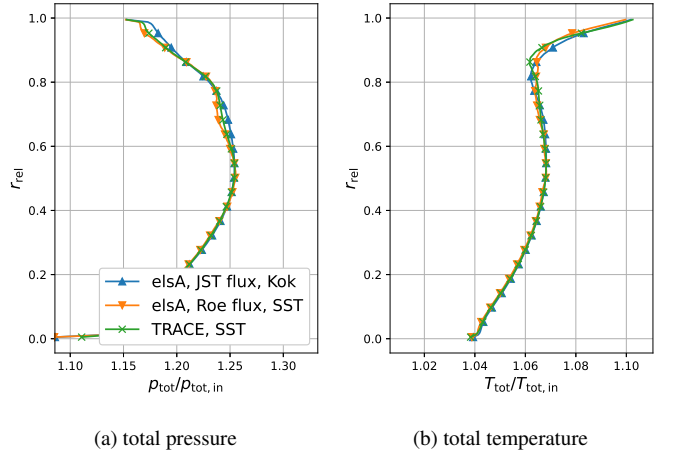


**FIGURE 5:** Radial distributions of absolute total quantities at analysis plane downstream of fan. Steady flows used to initialised frequency domain methods. (a) elsA solution used for Turb'Lin (b) elsA solution with Roe flux and configuration used for HB (c) TRACE setup used for HB.

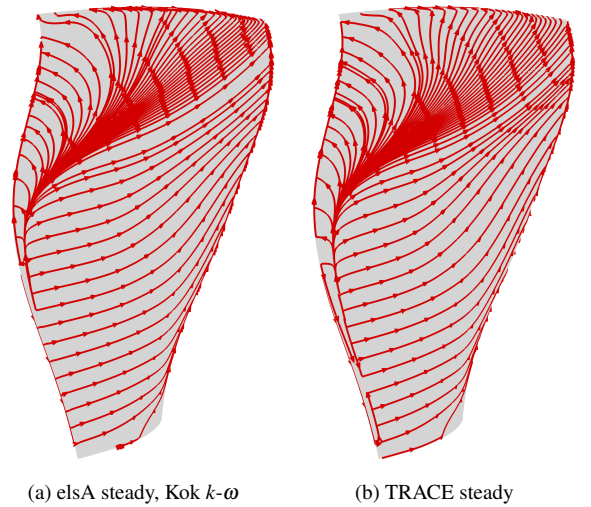
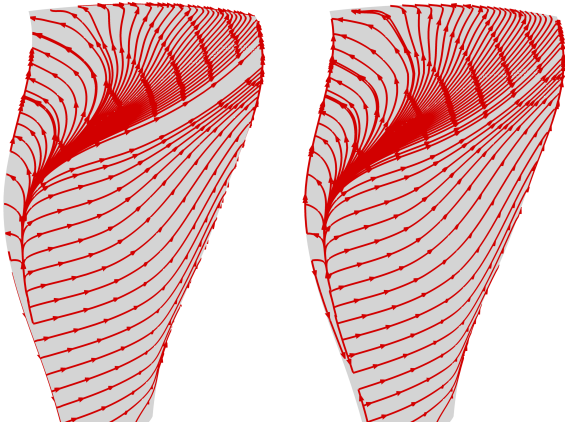


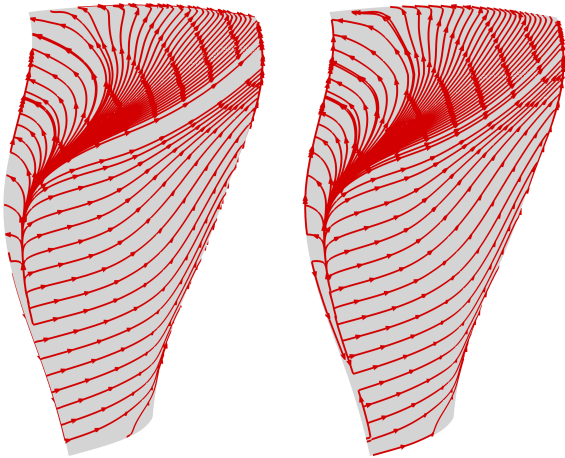
**FIGURE 6:** Streaklines on suction side. (a) Steady elsA solution used for Turb'Lin, (b) TRACE steady solution.

ND6. Both were obtained with the Roe solver and correspond to H01 setups. Comparison with the steady solver results shows that the unsteady effects for the given amplitude ( $a = 0.05$  mm) have little impact on mean shear stresses. Similarly, Figures 8 and 9 compare entropy distributions at 95% channel height for the steady and time-averaged flows. The agreement between TRACE and elsA, no matter which turbulence model is used, is very high. Figures 10 and 11 show the radial velocity component at the same location. These results show that the blockage



(a) elsA HB, Roe flux, ND5

(b) TRACE HB, H01, ND5



(c) elsA HB, Roe flux, ND6

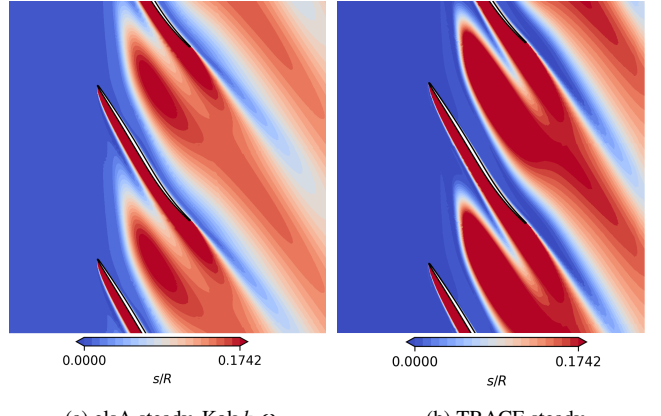
(d) TRACE HB, H01, ND6

**FIGURE 7:** Streaklines on suction side. Time-averaged HB flows for ND5 and ND6 (a) and (c) elsA HB with Roe solver, (c) and (d) TRACE HB H01.

at 95% channel height and the tip-leakage vortex trajectory are in good agreement. A very similar zone of separation and backflow is predicted by all methods and solver modes. Comparing TRACE steady and mean HB solutions for ND5 and ND6, one can conclude that the unsteady effect on the time-averaged flow in the passage is very limited for the given amplitude.

## 5 AERODYNAMIC DAMPING

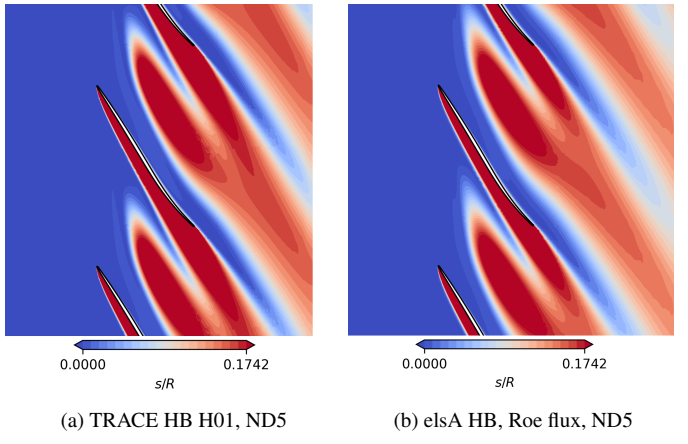
The flutter results are first compared in terms of the overall damping ratio predicted with the different solvers and setups. Figure 12 shows representative results for the three solvers. Though there is a slight offset between TRACE and elsA results



(a) elsA steady, Kok  $k-\omega$

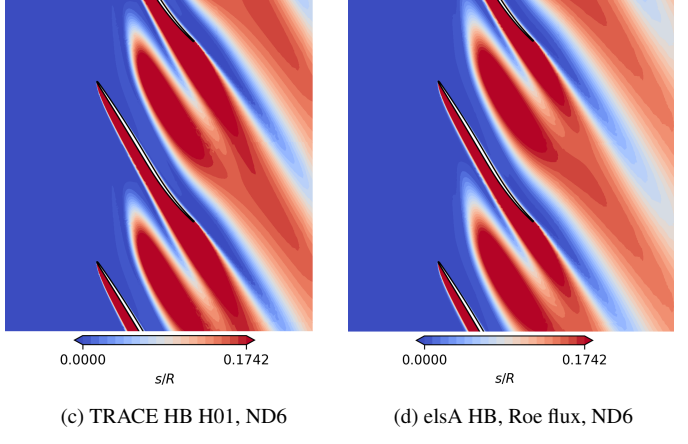
(b) TRACE steady

**FIGURE 8:** Entropy at 95% channel height. Steady flow solution with elsA (Kok model) and TRACE.



(a) TRACE HB H01, ND5

(b) elsA HB, Roe flux, ND5

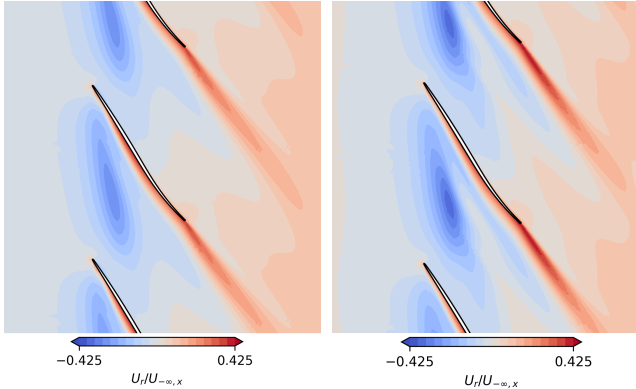


(c) TRACE HB H01, ND6

(d) elsA HB, Roe flux, ND6

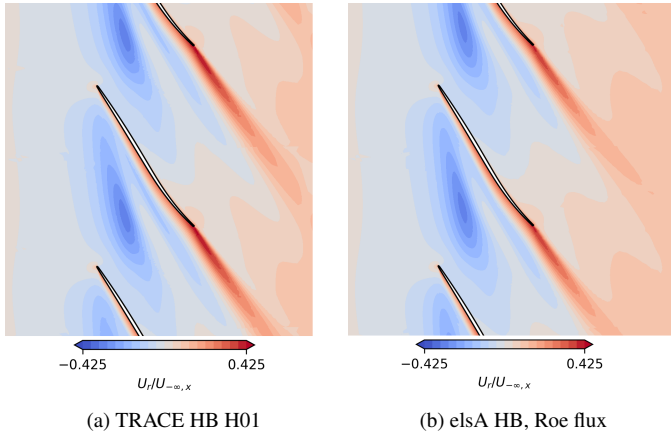
**FIGURE 9:** Entropy at 95% channel height. Mean flows for ND6. (a) TRACE H01 (b) elsA HB, Roe flux

for most nodal diameters both setups agree in that the damping



(a) elsA steady, Kok  $k-\omega$  (b) TRACE steady HB

**FIGURE 10:** Radial velocity at 95% channel height. Steady flow solution with elsA (Kok model) and TRACE.



(a) TRACE HB H01 (b) elsA HB, Roe flux

**FIGURE 11:** Radial velocity at 95% channel height. Mean flows for ND6. (a) TRACE H01 (b) elsA HB, Roe flux

ratio for ND5 is clearly positive and that the minimal damping is located at ND6. Note that this plot compares HB results with consistent setups, both are obtained with the Roe flux, Menter's SST model, an amplitude of 0.05 mm and an H01 setup.

Figure 13 compares the Turb'Lin results with TRACE setups H1 and H01. Since the mean flow in the H1 setup is the steady solution, this setup is comparable to that of a time-linearised approach. Indeed, when the mean flow is kept constant, then the harmonic balance solver also shows a minimal damping near ND5. For this setup, a frequency variation was performed in [3] which showed that the phase of the flow response was highly sensitive near the eigenfrequency for ND5. This was interpreted as convective resonance with a disturbance of relative circumferential speed of approximately  $-0.41\Omega$ . Whereas in [3] it was observed that the minimum near ND5 shifts to ND6 when an H01...5 setup is employed, the results in this work show that the

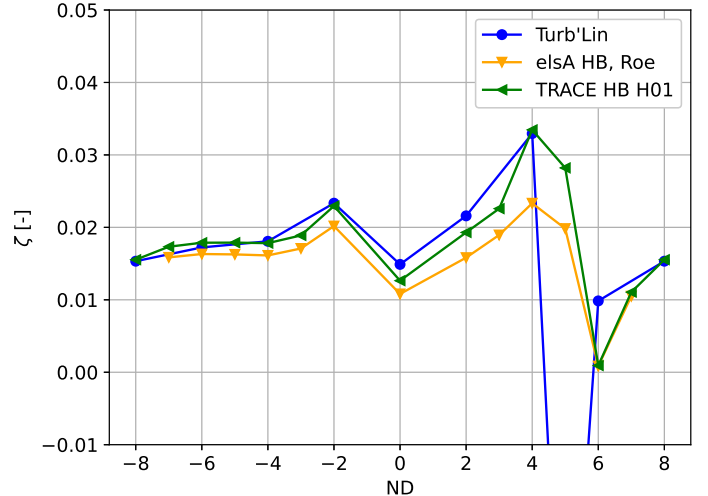


**FIGURE 12:** Aerodynamic damping ratio predicted by Turb'Lin, elsA HB and TRACE HB H01.

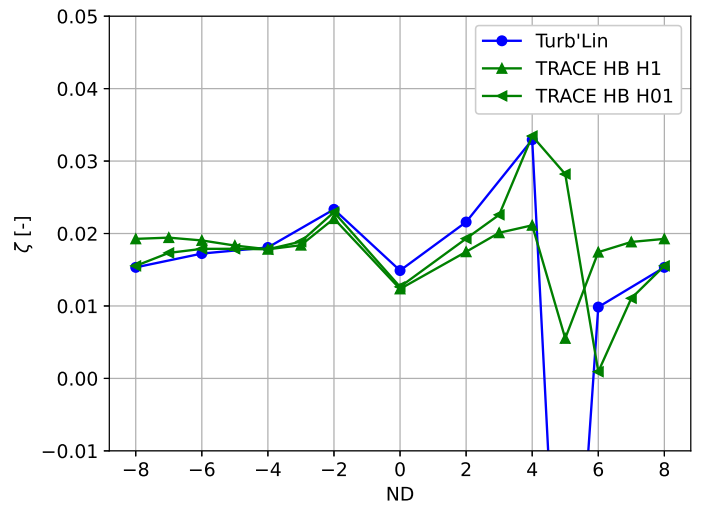


**FIGURE 13:** Aerodynamic damping ratio predicted by Turb'Lin and TRACE HB with and without coupling with mean flow (H01 and H1).

addition of the mean flow suffices to trigger this effect. The plot in Figure 14 compares the damping results obtained with TRACE of this work and the previous study. It can be seen that the damping values at ND4 to ND8 do change when higher harmonics are added. The global shape of the curve, however, remains unaffected.

The influence of the spatial discretisation scheme is illustrated by comparing the damping results obtained with elsA with the Roe flux and the two parameter sets for the Jameson-Schmidt-Turkel scheme. Similar to the above sensitivity to the

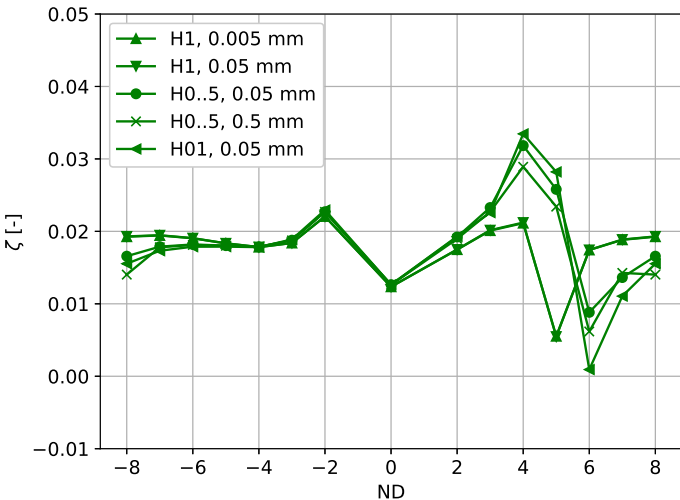


**FIGURE 14:** Aerodynamic damping ratio predicted by TRACE HB with different harmonic sets and amplitudes

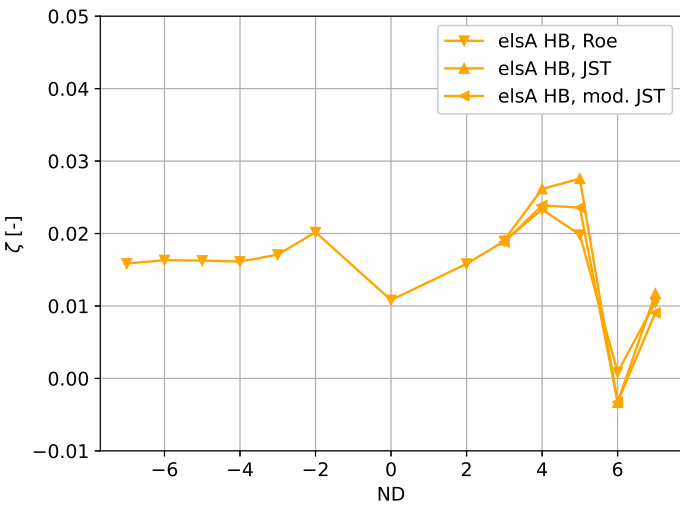


**FIGURE 15:** Aerodynamic damping ratio predicted by elsA HB with different setups

addition of harmonic, the spatial scheme does have an impact on the exact damping value with the damping for ND6 even being negative when the JST scheme is used. The shape of the damping curve does not depend on the spatial scheme though.

Figures 16 to 21 plot the aerodynamic damping ratio per area on the suction and pressure sides for the nodal diameters ND4, ND5 and ND6. The plots compare the elsA results obtained with the Roe flux. Again, there is a very high agreement between elsA and TRACE H01 which is in line with the above reasoning. For the nodal diameter of ND4 and 6, there is also a qualitative agreement between the surface data.

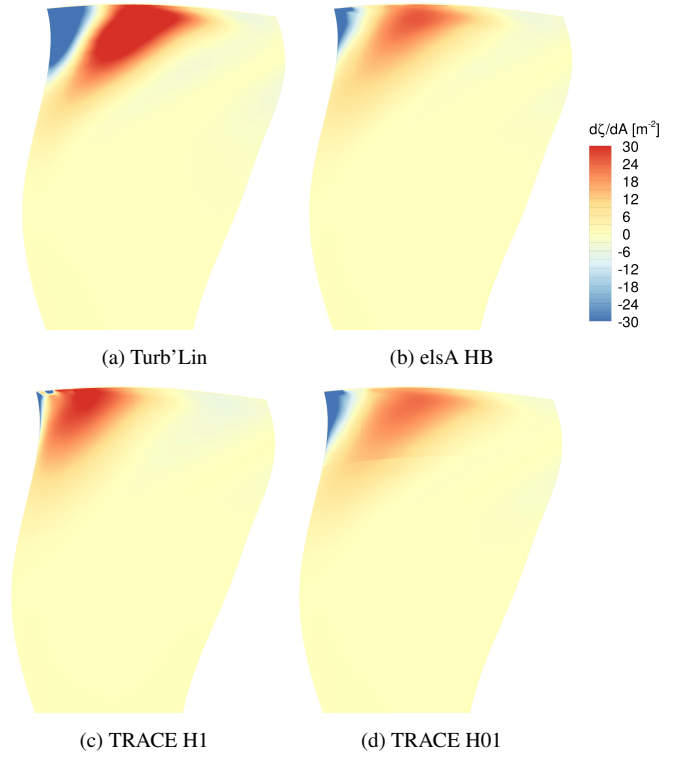


**FIGURE 16:** Work per area on suction side for ND4. elsA with Roe

## 6 DISCUSSION

The results presented above show that the harmonic flow response is highly sensitive to the treatment of the time average. In particular, the change of the mean flow due to nonlinear unsteady effects seems to cause a rise of the resonance frequency. Therefore, the relative circumferential flow velocity in the blade to blade surface at 95% has been plotted for the three solvers. Figure 10 shows results obtained with the steady setups used for the Turb'Lin and TRACE H1 results. The velocity fields have been normalised with the rotor speed at the given radius so that the freestream value is  $-1$ . Figure 23 depicts the time-averaged circumferential flow velocity for elsA and TRACE HB results, both for ND6, H01 setups and identical spatial schemes. These are in very high agreement and this was also confirmed for ND5, though the plots are not shown here. Moreover, the TRACE HB results for H01, when compared with the H1 setup show a higher contra-rotating relative velocity component. This can be seen in the difference plots in Figure 24 which are based on the HB H01 and steady TRACE results,

$$\Delta q = \bar{q}^{\text{HB}} - q^{\text{steady}}. \quad (15)$$

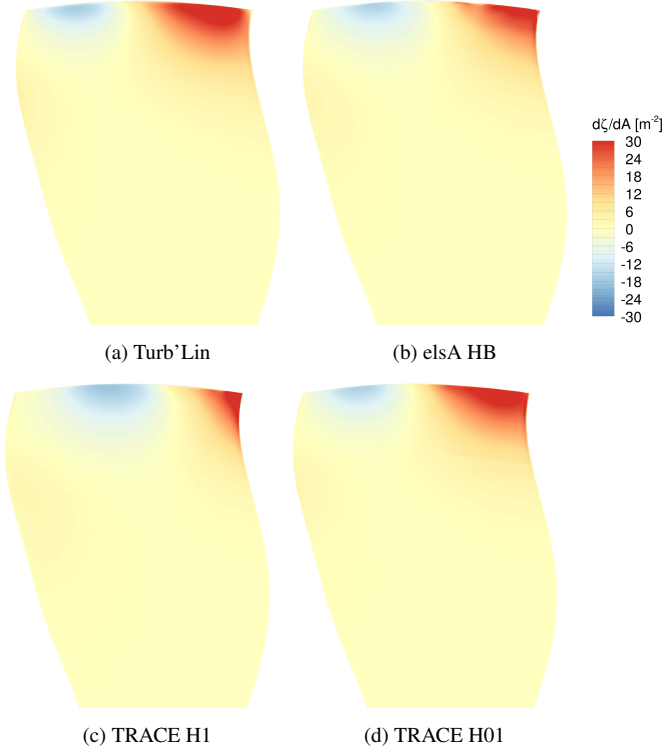


**FIGURE 17:** Work per area on pressure side for ND4. elsA with Roe

for ND5 and ND6. For both NDs an area of increased counter-rotating speed is observed in the blockage zone. To relate this to the apparent shift of the minimal damping from ND5 to ND6, note that the circumferential speed of a convective disturbance which is in resonance with a blade vibration that has angular frequency  $\omega_{\text{vib}}$  and nodal diameter ND must satisfy

$$\frac{\dot{\vartheta}_c}{\Omega} = -\frac{\omega_{\text{vib}}}{(ND - N)\Omega}, \quad (16)$$

cf. [3]. For ND = 5 this value is approximately  $-0.41$  whereas for ND = 6, it would be close to  $-0.45$ , see Fig. 25. The fact that the nodal diameter of 6 seems to be closer to resonance conditions can thus be explained by an increased relative circumferential flow speed which is clearly visible in Fig. 24 (blue areas).

For the operating point discussed here, Fiquet et al. [2] have run time-domain simulations both with fixed and vibrating blades. They inferred from the results with fixed blades that the convective disturbances travel with a speed of  $-0.45\Omega$  in circumferential direction. The critical nodal diameter for non-synchronous vibrations of Mode 2 in this operating point would therefore be 6 rather than 5. This is in line with the HB results presented in this study. The aerodynamic damping values found

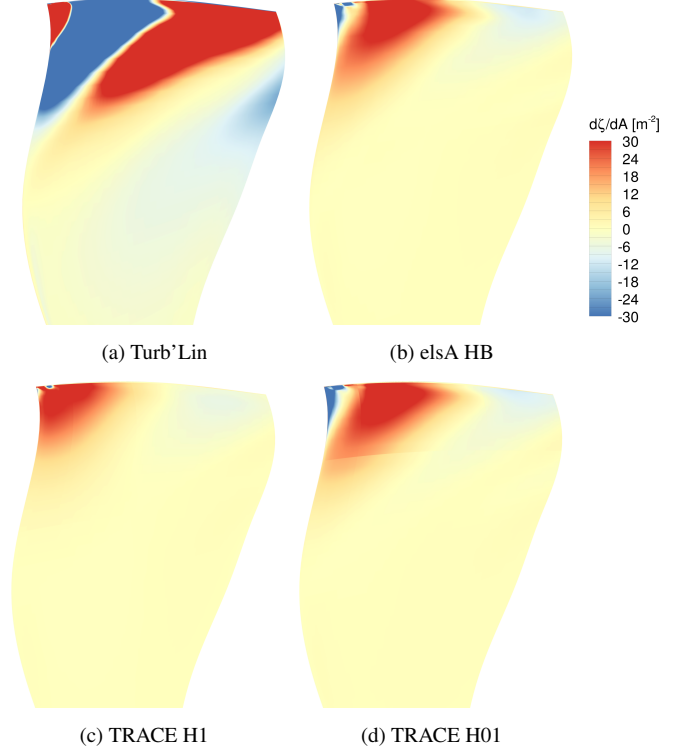


**FIGURE 18:** Work per area on suction side for ND5. elsA with Roe

ND	4	5	6
$\zeta$ (in %)	1.57	1.67	1.82

**TABLE 2:** Damping ratios obtained with elsA time-marching and prescribed blade vibration, from [2]

by Fiquet et al. are given in Table 2. These results are coherent with the HB results presented here for ND4 and ND5 in that a clearly positive damping ratio in the order of 2% is observed which rules out significant blade vibrations in these NDs. The time-domain results for ND6 showed no drop in damping which is somewhat contradicting the results presented in this work. It should be emphasised, however, that the time-domain computational domain included a spherical air intake. As was observed in [1], the eigenfrequency of Mode 2 is very close to the cut-on/cut-off boundary for circumferential mode order 6 at the inlet. Therefore, interactions with the intake can alter significantly the results. Note also that the TRACE HB results with an HB0...5 setup showed a considerable increase in damping compared to H01, see Fig. 14. This indicates that higher harmonics, which are inherently resolved in time-marching simulations, may play a crucial role for the first harmonic flow response.

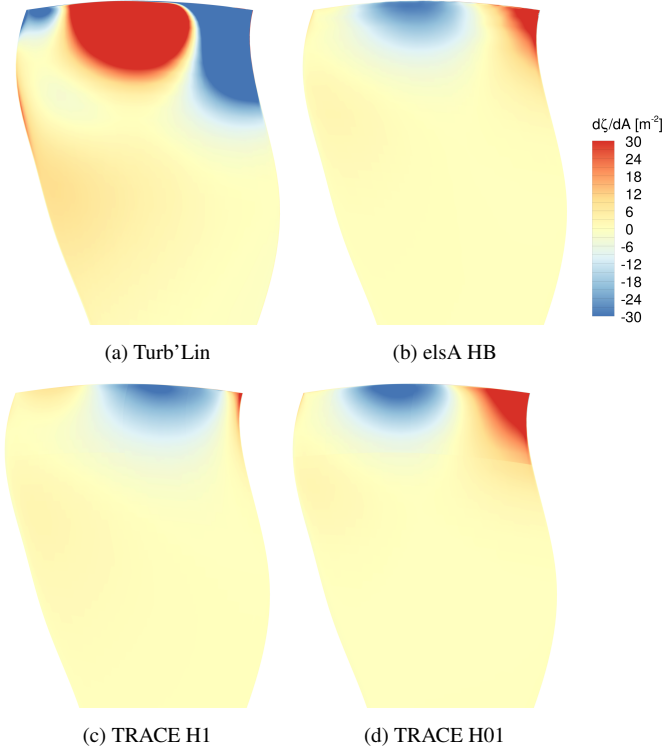


**FIGURE 19:** Work per area on pressure side for ND5. elsA with Roe

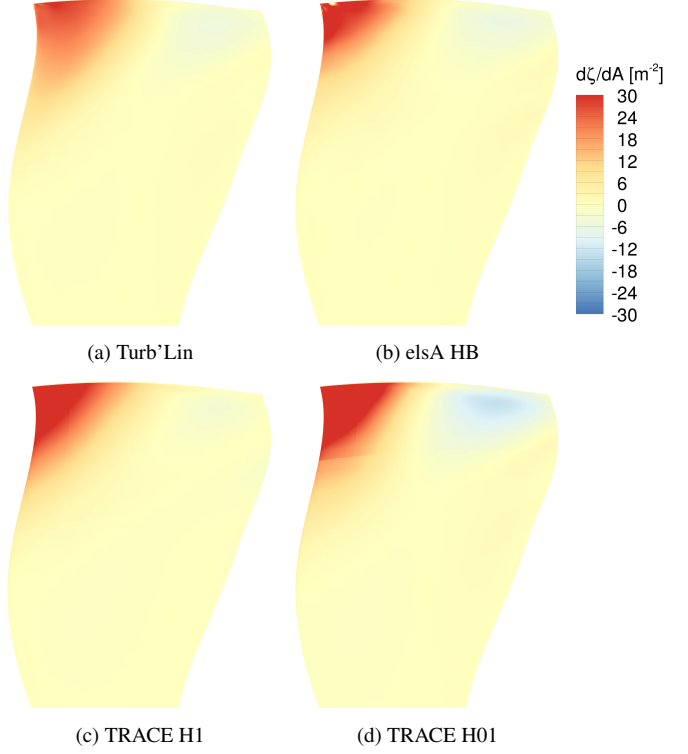


**FIGURE 20:** Work per area on suction side for ND6. elsA with Roe

## 7 SUMMARY AND CONCLUSION

In this paper, CFD results obtained with three different solvers have been shown to give relatively consistent results for the flutter analysis of a fan at off-design conditions. This is all the more remarkable as past attempts to consolidate flutter results from different CFD methods resulted in much greater discrepancies (see e.g. [30] for a comparison of aerodynamic damping for the TU Darmstadt compressor).

The results show that with an equivalent setup, the harmonic balance and the time-linearised methods give very similar results. As was observed in our earlier study [3], the characteristic circumferential speed of the convective disturbances can thus be estimated on the basis of linearised approaches. The latter quantity is a crucial parameter to predict the possible onset of non-synchronous vibrations, which, for the ECL5/CATANA fan were observed in experiments for lower mass flows. The results in this paper, however, show that the nodal diameter, for which the damping is minimal, corresponds to normalised relative circumferential speeds close to  $-0.45$  rather than the value of  $-0.41$  which was found for frozen mean flow. The results obtained with the harmonic balance solver in elsA confirmed this trend and showed that it did not depend on the spatial discretisation scheme. Whereas our previous study revealed a similar shift of

the minimal damping from ND5 to ND6, the results here demonstrate that computing the mean flow with the harmonic balance solver suffices to observe this behaviour. A comparison of the steady to the time-averaged harmonic balance TRACE results indicated that a cause might be the significant change of the mean circumferential flow velocity.

## REFERENCES

- [1] Pagès, V., Duquesne, P., Aubert, S., Blanc, L., Ferrand, P., Ottavy, X., and Brandstetter, C., 2022. “UHBR open-test-case fan ECL5/CATANA”. *International Journal of Turbomachinery, Propulsion and Power*, 7(2).
- [2] Fiquet, A.-L., Ottavy, X., and Brandstetter, C., 2024. “UHBR open-test case fan ECL5/CATANA: Non-linear analysis of non-synchronous blade vibration at part-speed conditions”. *Journal of Turbomachinery*, 146(7).
- [3] Frey, C., Aubert, S., Ferrand, P., and Fiquet, A.-L., 2025. “Flutter analysis of the ECL5 open fan testcase using harmonic balance”. *International Journal of Turbomachinery, Propulsion and Power*. to appear.
- [4] Duquesne, P., Rendu, Q., Aubert, S., and Ferrand, P., 2019. “Choke flutter instability sources tracking with linearized

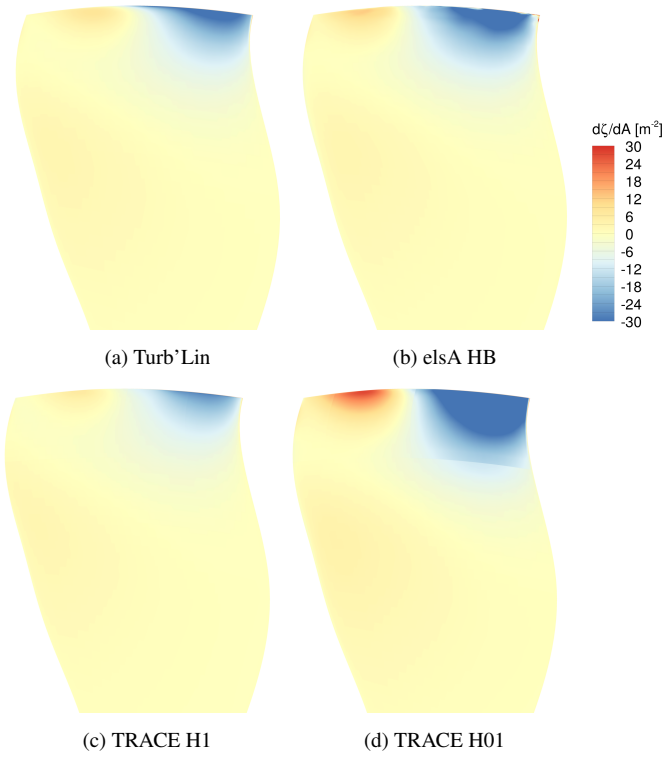


**FIGURE 21:** Work per area on pressure side for ND6. elsA with Roe

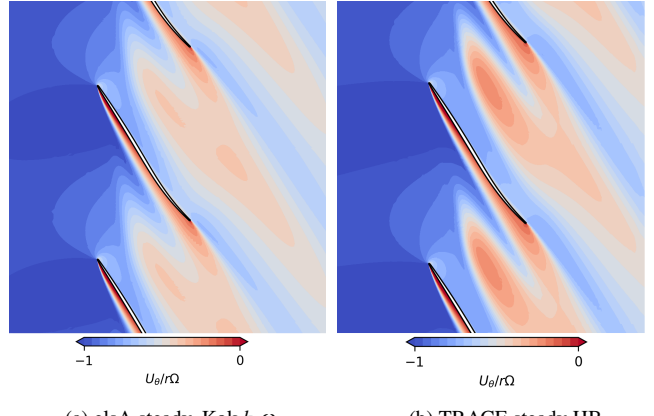


**FIGURE 22:** Relative circumferential velocity at 95% channel height, non-dimensionalised with rotor speed. Steady flow solution with elsA (Kok model) and TRACE.

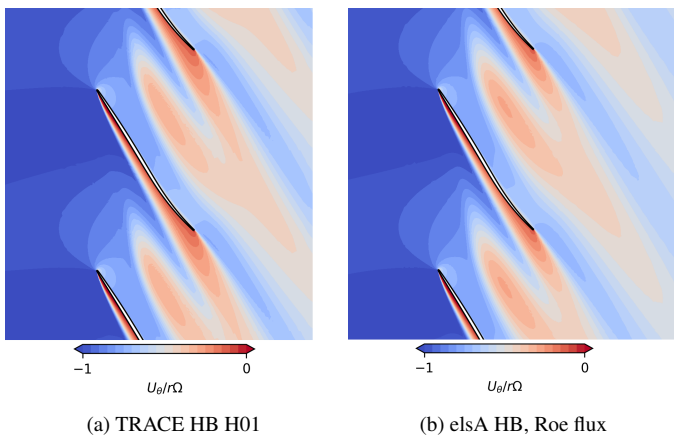


**FIGURE 23:** Relative circumferential velocity at 95% channel height, non-dimensionalised with rotor speed. Mean flows for ND6. (a) TRACE H01 (b) elsA HB, Roe flux

calculations”. *International Journal of Numerical Methods for Heat & Fluid Flow*, 06.

[5] Gilmore, R. J., and Steer, M. B., 1991. “Nonlinear circuit analysis using the method of harmonic balance - a review of the art. Part I. Introductory concepts”. *International Journal of Microwave and Millimeter-Wave Computer-Aided Engineering*, 1(1), pp. 22–37.

[6] Gilmore, R. J., and Steer, M. B., 1991. “Nonlinear circuit analysis using the method of harmonic balance - a review of the art. Part II. Advanced concepts”. *International Journal of Microwave and Millimeter-Wave Computer-Aided Engineering*, 1(2), pp. 159–180.

[7] Sicot, F., Guedeney, T., and Dufour, G., 2013. “Time-domain harmonic balance method for aerodynamic and aeroelastic simulations of turbomachinery flows”. *Int. J. Comput. Fluid D.*, 27(2), Feb., pp. 68–78.

[8] Hall, K. C., Thomas, J. P., and Clark, W. S., 2002. “Computation of unsteady nonlinear flows in cascades using a harmonic balance technique”. *AIAA J.*, 40(5), May, pp. 879–886.

[9] McMullen, M., Jameson, A., and Alonso, J., 2006. “Demonstration of nonlinear frequency domain methods”. *AIAA Journal*, 44(7), July, pp. 1428–1435.

[10] Frey, C., Ashcroft, G., Kersken, H.-P., and Voigt, C., 2014. “A harmonic balance technique for multistage turbomachinery applications”. In ASME Turbo Expo 2014: Turbine Technical Conference and Exposition, no. 45615, p. V02BT39A005.

[11] Frey, C., Backhaus, J., Ashcroft, G., Geiser, G., Winhart, B., and Stüber, H., 2025. “Using pseudotime marching for the solution of harmonic balance problems”. *Journal of Turbomachinery*, 147(9), 02, p. 091007.

[12] Cambier, L., Gazaix, M., Heib, S., Plot, S., Poinot, M., Veuillot, J., Boussuge, J.-F., and Montagnac, M., 2011. “CFD platforms and coupling : An overview of the multi-purpose elsA flow solver”. *Aerospace Lab*, Issue 2, 03.

[13] Roe, P. L., 1981. “Approximate Riemann solvers, param-

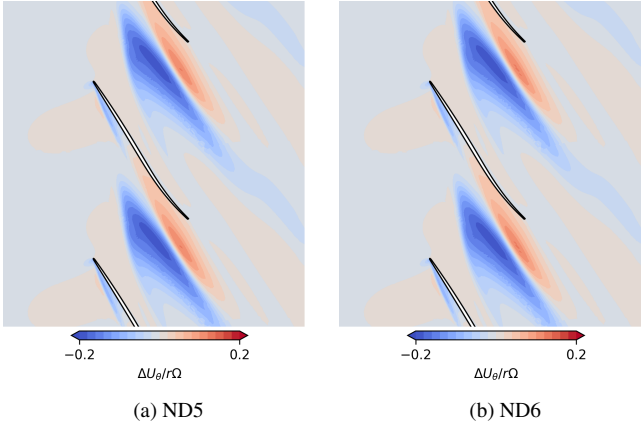


**FIGURE 24:** Difference between harmonic balance mean flow and steady flow, non-dimensionalised with rotor speed, at 95% channel height, (a) ND5 (b) ND6

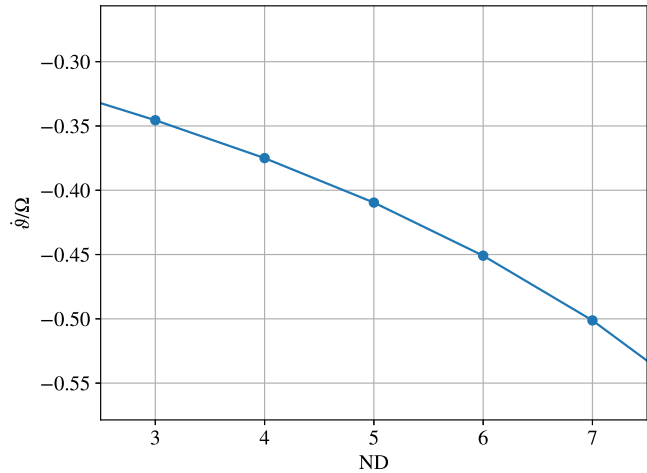


**FIGURE 25:** Relative circumferential speed of a convective disturbance that is in resonance with a certain nodal diameter for the second blade eigenmode.

eter vectors, and difference schemes”. *J. Comput. Phys.*, 43(2), pp. 357 – 372.

[14] van Albada, G. D., van Leer, B., and Roberts, Jr., W. W., 1982. “A comparative study of computational methods in cosmic gas dynamics”. *Astron. Astrophys.*, 108(1), April, pp. 76–84.

[15] Blazek, J., 2001. *Computational fluid dynamics: principles and applications*. Elsevier Science.

[16] Menter, F., Kuntz, M., and Langtry, R., 2003. “Ten years of industrial experience with the SST model.”. In *Turbulence, Heat and Mass Transfer 4*, K. Hanjalić, Y. Nagano,

and M. Tummers, eds.

[17] Kok, J. C., 2000. “Resolving the dependence on freestream values for the  $k-\omega$  turbulence model”. *AIAA Journal*, 38(7), pp. 1292–1295.

[18] Menter, F., 1992. Improved two-equation  $k-\omega$  turbulence models for aerodynamic flows. Technical Memorandum 103975, NASA Ames Research Center, Moffett Field, CA, USA, October.

[19] Dufour, G., Sicot, F., Puigt, G., Liauzun, C., and Dugeai, A., 2010. “Contrasting the harmonic balance and linearized methods for oscillating-flap simulations”. *AIAA Journal*, 48(4), pp. 788–797.

[20] Sicot, F., Dufour, G., and Gourdain, N., 2012. “A time-domain harmonic balance method for rotor/stator interactions”. *J. Turbomach.*, 134(1), p. 011001.

[21] Kato, M., and Launder, B. E., 1993. “The modeling of turbulent flow around stationary and vibrating square cylinders”. In *9th Symposium on Turbulent Shear Flows*, pp. 10.4.1–10.4.6.

[22] Müller, M., Kersken, H.-P., and Frey, C., 2022. “A log-w turbulence model formulation for flutter analysis with harmonic balance”. In *16th International Symposium on Unsteady Aerodynamics, Aeroacoustics & Aeroelasticity of Turbomachines ISUAAAT16* (to appear).

[23] Ashcroft, G., Frey, C., and Kersken, H.-P., 2014. “On the development of a harmonic balance method for aeroelastic analysis”. In *6th European Conference on Computational Fluid Dynamics (ECFD VI)*, pp. 5885–5897.

[24] Frey, C., Ashcroft, G., Kersken, H.-P., and Schlüß, D., 2019. “Flutter analysis of a transonic steam turbine blade with frequency and time-domain solvers”. In *13th European Turbomachinery Conference on Turbomachinery Fluid Dynamics and Thermodynamics, ETC 2019*.

[25] Rendu, Q., Philit, M., Labit, S., Chassaing, J.-C., Rozenberg, Y., Aubert, S., and Ferrand, P., 2015. “Time-linearized and harmonic balance navier-stokes computations of a transonic flow over an oscillating bump”. In *Proceedings of the 14th International Symposium on Unsteady Aerodynamics, Aeroacoustics & Aeroelasticity of Turbomachines ISUAAAT14*.

[26] Kersken, H.-P., Frey, C., Voigt, C., and Ashcroft, G., 2012. “Time-linearized and time-accurate 3D RANS methods for aeroelastic analysis in turbomachinery”. *J. Turbomach.*, 134(5), p. 051024.

[27] Philit, M., Ferrand, P., Labit, S., Chassaing, J.-C., Aubert, S., and Fransson, T., 2012. “Derivated turbulence model to predict harmonic loads in transonic separated flows over a bump”. *28th Congress of the International Council of the Aeronautical Sciences 2012, ICAS 2012*, 4, 01, pp. 2713–2723.

[28] Rodrigues, M., Soulard, L., Paoletti, B., Ottavy, X., and Brandstetter, C., 2021. “Aerodynamic Investigation of a

Composite Low-Speed Fan for UHBR Application”. *Journal of Turbomachinery*, 143(10), p. 101004.

[29] Kersken, H.-P., Ashcroft, G., Frey, C., Wolfrum, N., and Korte, D., 2014. “Nonreflecting boundary conditions for aeroelastic analysis in time and frequency domain 3D RANS solvers”. In Proceedings of ASME Turbo Expo 2014.

[30] Fransson, T., 2013. Flutter-Free Turbomachinery Blades (FUTURE), Final Report. EU grant agreement ID: 213414. <https://cordis.europa.eu/docs/results/213414/final1-ftr-5-93.pdf>. Accessed: 05 Sep 2025.